Noninvasive two-photon optical biopsy of retinal fluorophores

Grazyna Palczewska[a,b], Jakub Boguslawski[c], Patrycjusz Stremplewski[d], Lukasz Kornaszewski[c], Jianye Zhang[b], Zhiqian Dong[a,b], Xiao-Xuan Liang[e], Enrico Gratton[f], Alfred Vogel[e,1], Maciej Wojtkowski[c,1], and Krzysztof Palczewski[b,g,h,1]

[a]Department of Medical Devices, Polgenix, Inc., Cleveland, OH 44106; [b]Gavin Herbert Eye Institute, Department of Ophthalmology, University of California, Irvine, CA 92697; [c]International Centre for Translational Eye Research, Institute of Physical Chemistry, Polish Academy of Sciences, 01-224 Warsaw, Poland; [d]Faculty of Physics, Nicolaus Copernicus University, 87-100 Torun, Poland; [e]Institute of Biomedical Optics, University of Luebeck, 23562 Luebeck, Germany; [f]Department of Biomedical Engineering, University of California, Irvine, CA 92697; [g]Department of Physiology & Biophysics, University of California, Irvine, CA 92697; and [h]Department of Chemistry, University of California, Irvine, CA 92697

Edited by Janet R. Sparrow, Columbia University Medical Center, New York, NY, and accepted by Editorial Board Member Jeremy Nathans July 27, 2020 (received for review April 19, 2020)

High-resolution imaging techniques capable of detecting identifiable endogenous fluorophores in the eye along with genetic testing will dramatically improve diagnostic capabilities in the ophthalmology clinic and accelerate the development of new treatments for blinding diseases. Two-photon excitation (TPE)-based imaging overcomes the filtering of ultraviolet light by the lens of the human eye and thus can be utilized to discover defects in vitamin A metabolism during the regeneration of the visual pigments required for the detection of light. Combining TPE with fluorescence lifetime imaging (FLIM) and spectral analyses offers the potential of detecting diseases of the retina at earlier stages before irreversible structural damage has occurred. The main barriers to realizing the benefits of TPE for imaging the human retina arise from concerns about the high light exposure typically needed for informative TPE imaging and the requirement to correlate the ensuing data with different states of health and disease. To overcome these hurdles, we improved TPE efficiency by controlling temporal properties of the excitation light and employed phasor analyses to FLIM and spectral data in mouse models of retinal diseases. Modeling of retinal photodamage revealed that plasma-mediated effects do not play a role and that melanin-related thermal effects are mitigated by reducing pulse repetition frequency. By using noninvasive TPE imaging we identified molecular components of individual granules in the retinal pigment epithelium and present their analytical characteristics.

eye | retina | two-photon | imaging | RPE

The transparency of the anterior segment of the eye provides a unique opportunity for identifying vital molecular events within the retina and retinal pigment epithelium (RPE) which contribute to human vision in health and disease. Noninvasive optical imaging not only can reveal these important mechanisms but also can help accelerate the development of therapies against debilitating blinding diseases. For example, advances in optical coherence tomography (OCT) (1) and fundus imaging enabled the identification of structural changes to the retina during disease progression (2, 3). However, there is a need for noninvasive imaging of the eye that can assess not only structural changes but also biochemical processes, such as the trafficking and transformation of vitamin A metabolites indispensable for vision. Considering the absorption spectra of retinyl esters and the transmission properties of the human lens and cornea (4–6), two-photon excitation (TPE) imaging utilizing near infrared (IR) light is ideally suited for visualizing the transformation and distribution of metabolic components in the retina and RPE.

TPE imaging of the eye was initially employed during the discovery of lipid droplets, termed retinosomes, which contain highly concentrated retinyl esters (7). It was then demonstrated in vivo that retinosomes participate in the formation of the visual chromophore 11-*cis*-retinal, opening the possibility that this process could be imaged in vivo at the subcellular level. In further imaging experiments with different mouse models, it was shown that retinosomes overaccumulate in $Rpe65^{-/-}$ mice and that they are absent in the eyes of $Lrat^{-/-}$ mice which are deficient in retinyl ester synthesis and thus lack visual chromophores and consequently are deprived of visual function (8, 9). Further advances in TPE imaging led to the characterization of retinal condensation products in mouse models of light-induced retinal degeneration and the evaluation of drug candidates mitigating the effects on photoreceptor survival (4, 10, 11).

In most cases TPE fluorescence imaging requires exposures to high-intensity IR laser light. Furthermore, collection of fluorescence lifetime imaging (FLIM) and hyperspectral data over a large area involves long acquisition time and/or high laser light exposure to enable identification of fluorescent granules within retinal cells based on the fluorescence properties of their components. Moreover, noninvasive mapping of the subcellular distribution of endogenous fluorophores based on their spectral and decay data in the eyes of mouse models of retinal diseases is lacking. These are limiting factors for realizing the many benefits

Significance

Two-photon excitation (TPE) of retinal fluorophores with infrared light allows monitoring metabolic transformation of the retina. TPE imaging can provide information about biochemical events that precede structural damage to the retina and thereby accelerate the development of therapies against blinding diseases. While subcellular TPE of endogenous retinoids in the retina and retinal pigment epithelium of mice and nonhuman primates has been achieved, TPE imaging of the human retina has not been fully realized due to concerns about safety and identity of molecular signals. We therefore improved TPE efficiency by controlling temporal properties of the excitation light, performed extensive modeling of nonlinear damage mechanisms, and identified molecular components of individual RPE granules in mouse models of retinal diseases employing phasor analyses.

Author contributions: G.P., J.B., P.S., X.-X.L., A.V., M.W., and K.P. designed research; G.P., J.B., P.S., L.K., J.Z., Z.D., X.-X.L., and A.V. performed research; G.P., J.B., L.K., X.-X.L., E.G., A.V., M.W., and K.P. analyzed data; and G.P., E.G., A.V., M.W., and K.P. wrote the paper.

Competing interest statement: K.P. is Chief Scientific Officer at Polgenix, Inc. K.P. is also an inventor of the US patent no. 7,706,863 and US patent no. 8,346,345, whose values may be affected by this publication. G.P. and Z.D. are employees of Polgenix, Inc.

This article is a PNAS Direct Submission. J.R.S. is a guest editor invited by the Editorial Board.

[1]To whom correspondence may be addressed. Email: alfred.vogel@uni-luebeck.de, kpalczew@uci.edu, or mwojtkowski@ichf.edu.pl.

This article contains supporting information online at https://www.pnas.org/lookup/suppl/doi:10.1073/pnas.2007527117/-/DCSupplemental.

First published August 26, 2020.

that TPE offers to image the retina and RPE in humans, the most critical of which is that the exposure to IR laser light must be minimized to ensure lack of damage during and after the imaging session. The interpretation of data needs to be supplemented by the spectral identification of fluorescent compounds and confirmed by noninvasive imaging of mice which replicate some features of retinal diseases. In this study we used *Abca4*$^{PV/PV}$*Rdh8*$^{-/-}$ mice which have mutations in the ABCA4 transporter and a retinol dehydrogenase that result in elevated levels of fluorescent diretinoid-pyridiniumethanolamine (A2E) as well as *Rpe65*$^{-/-}$ mice which carry a mutation in a critical retinoid isomerase and replicate the human form of Leber congenital amaurosis (12, 13). Considering that for a given average power the TPE fluorescence rate is inversely proportional to the pulse duration and pulse repetition frequency (PRF) (14–18), we previously demonstrated over a 300% increase in fluorescence for the same average power by reducing the pulse duration from 75 to 20 fs and incorporating phase modulation of the spectral components of the excitation light to achieve high-order dispersion compensation (14, 19). However, reduction of pulse duration is concomitant with an increase of spectral bandwidth. Thus, bandwidths associated with pulses shorter than ∼20 fs exceed the absorption band of informative retinal fluorophores, and two-photon (TP) absorption as a function of inversed pulse duration tends to saturate after crossing a certain value which is approximately the linewidth of the absorption spectrum of the dye (20). Because further reduction of pulse duration would be counterproductive, we developed a TPE imaging system with reduced PRF (Fig. 1*A*). In this study, using noninvasive techniques, we report the molecular identification, localization, and quantification of eye cellular components based on the increased efficiency of TPE fluorescence generation from intrinsic retinal fluorophores using advanced methods for fluorescence signal processing. We measured fluorescence decay and spectral data to noninvasively distinguish and differentiate vitamin A stores and deposits of retinoid cycle byproducts at subcellular resolution in mouse eyes and how they are impacted by genetic manipulations to replicate conditions associated with blinding diseases in humans. Furthermore, we evaluated possible photodamage pathways by numerical simulations.

Results

The data from the eyes of well-characterized genetic background mouse lines were compared with authentic standards using spectrally sensitive fluorescent excitation and emission conditions. Moreover, we explored melanin interference in obtaining high-resolution imaging.

TPE of Synthetic Standards Relevant to Retina Imaging. After incorporating pulse selection capabilities into the TPE imaging system, we measured the fluorescence of synthetic A2E (Fig. 1 *A* and *B*), one of the main condensation products of vitamin A metabolites present in the eye, and retinyl palmitate, a main component of retinosomes (*SI Appendix*, Fig. S1), as a function of the power of 850 and 750 nm light in response to 80- and 8-MHz excitation. For A2E, slopes of the linear regression lines on the log-log plot fitted to 8- and 80-MHz data were equal to 2, and for retinyl palmitate slopes were 1.5 for 8-MHz and 1.9 for 80-MHz data, both indicating a nonlinear second-order process. Additionally, we obtained TPE fluorescence lifetime, phasor signatures, and spectral data for these compounds with different wavelengths (Fig. 1 *C* and *D*). We used fluorescein at pH 9.4 as a reference. To our knowledge the literature does not contain adequate TPE fluorescence lifetime data on retinyl esters and A2E solutions.

As expected, fluorescein phasor points were located on the circumference line of the universal semicircle indicating a monoexponential decay and its fluorescence lifetime was 4.4 ns for excitation wavelengths of 780 and 850 nm. However, the phasor points for A2E and retinyl palmitate were located inside the universal semicircle, which indicates that both compounds had a multiexponential decay (Fig. 1*C*) (21). When changing the excitation wavelength from 750 to 780 nm, the fluorescence lifetime of retinyl palmitate and the location of its phasor points

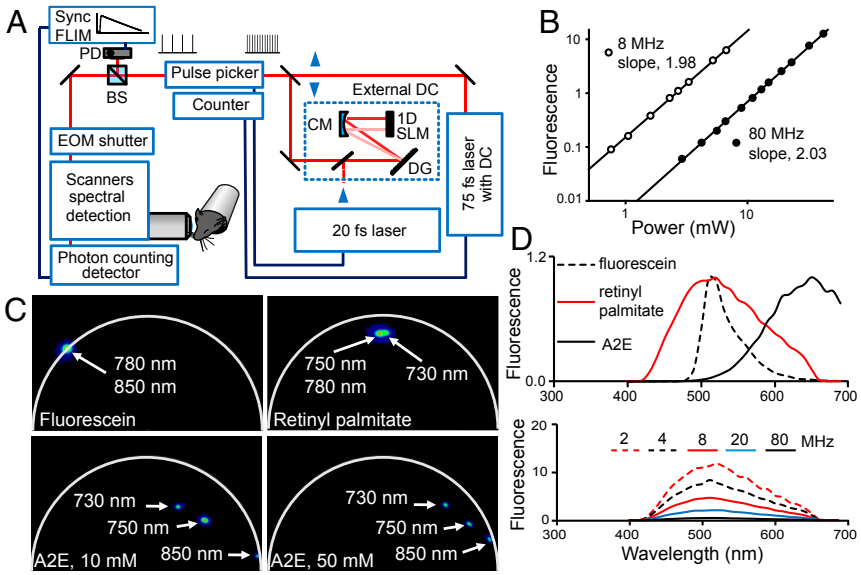

Fig. 1. TPE with reduced PRF. (*A*) Depiction of the TPE fluorescence imaging system equipped with 75- and 20-fs lasers, high-order dispersion compensation (DC), pulse selection system, and synchronization (Sync) for FLIM. DG, diffraction grating; CM, concave mirror; 1D SLM, one-dimensional spatial light modulator; BS, beam splitter; PD, photodiode; EOM, electro-optic modulator. (*B*) Fluorescence of 20 mM A2E in mean photon counts per pixel as a function of 850-nm excitation light power. Slopes of linear regression lines through the data points on the log-log plots indicate TPE fluorescence for both 80- and 8-MHz PRF. (*C*) FLIM semicircle phasor plots of synthetic compounds relevant to retinal fluorophores: A2E in DMSO with molar concentrations indicated in panels and pure retinyl palmitate, 1.75 M; fluorescein in 100 mM sodium borate, pH 9.5, is included as a control. Clusters of phasor points are color mapped from blue to red, such that red represents highest pixel density. (*D*, *Upper*) Normalized TPE fluorescence spectra of pure 1.75-M retinyl palmitate, 10 mM A2E in DMSO, and fluorescein in 100 mM sodium borate, pH 9.5. (*D*, *Lower*) Fluorescence spectral shape of retinyl palmitate does not change with PRF.

did not change substantially. Analyses of fluorescence decay data fitted by a three-exponent model function revealed an amplitude weighted fluorescence lifetime (τ_m) expressed by *SI Appendix*, Eq. **S1** to be 1.6 ns. Previously, measured by one-photon excitation, the fluorescence lifetime of retinyl palmitate in liposomes was 2.17 ns (22, 23). A two-exponent model function was adequate to fit A2E decay data. The τ_m of synthetic A2E dissolved in dimethyl sulfoxide (DMSO) varied with A2E concentration and with excitation wavelengths. At 10-mM concentration and 750-nm excitation the τ_m was 0.30 ns and for 850 nm it was 0.14 ns, obtained by the amplitude weighted fit of fluorescent decay lifetimes modeled by two exponents. Previous studies reported an A2E fluorescence lifetime of 0.19 ns for a two-exponent fit and single-photon excitation at 446 nm (24), while TP excitation with 1,070 nm light yielded a lifetime value of 0.17 ns for emission wavelengths in the range of 600 to 670 nm (25).

The fluorescence emission maximum for fluorescein was at 510 nm for excitation wavelengths from 488 (one photon) to 850 nm. Fluorescence emission spectra of retinyl palmitate did not change in response to excitation in the range of 730 to 780 nm and had a maximum at 515 nm (Fig. 1*D*). Its 850-nm excited fluorescence was too weak to provide a robust measurement of the emission spectra. Furthermore, the shape of the TPE emission spectra of retinyl palmitate did not change with PRF in response to 2-mW excitation with 750 nm light. The amount of fluorescence increased as the PRF decreased. The rate of increase was lower for PRF less than 8 MHz. The A2E fluorescence maximum occurred at 650 nm for excitation with 850 nm light. In brief, we demonstrated that TP fluorescence increases with reduced PRF and we obtained fluorescence spectral and decay characteristics of synthetic fluorophores relevant to imaging the retina and RPE.

RPE Subcellular Map of Various Retinoids in Mouse Models Based on Intrinsic Fluorescence. Considering that *Rpe65*$^{-/-}$ mice do not accumulate A2E and overaccumulate retinyl esters in their RPE (26, 27), we first obtained phasor plots of the RPE in intact mouse eyes (Fig. 2*A*). The phasor plot showed a very tight distribution of pixels in the same region as that obtained for pure retinyl palmitate (Fig. 1*C*). Moreover, a comparison of the intensity-based image with the FLIM image, based on a color scale assigned per triangle indicated in the phasor plot, unequivocally demonstrated that all fluorescent granules in the RPE contained retinyl esters, consistent with the distribution of retinosomes in previous reports (4, 7).

To visualize retinal condensation products in the RPE, we studied *Abca4*$^{PV/PV}$*Rdh8*$^{-/-}$ mice, which were shown previously to accumulate A2E (12). We obtained FLIM images using 850 nm light (Fig. 2*B*), because no excitation at that wavelength was expected for retinyl esters (4, 14). The phasor plot again showed a very tight distribution of pixels, but this time located at the right corner of the semicircle plot, consistent with the A2E phasor plot at that excitation wavelength, as shown in Fig. 1*C*. Furthermore, the FLIM image revealed that the entire interior of the RPE cell, except for the nucleus and pixels located near the RPE cell borders, was filled with fluorescent compounds responding to 850 nm light and having fluorescence lifetime properties associated with A2E. These data suggest that there is no accumulation of this fluorophore within subcellular structures as previously suggested (28, 29).

To determine whether the localization of retinyl esters is perturbed in the RPE of *Abca4*$^{PV/PV}$*Rdh8*$^{-/-}$ mice, we collected images using 730 nm light (Fig. 2*C*). Under these conditions the phasor plot showed a multitude of phasor point locations (*SI Appendix*, Fig. S2*A*). There were four clusters of phasor points: 1) a grouping of points in the region of the retinosome phasor cluster shown in Fig. 2*A*; 2) a grouping of points in the region of the 730-nm excitation A2E phasor cluster shown in Fig. 1*C*; 3) a grouping of points indicating image pixels that contained contributions from both types of fluorophores, i.e., retinyl esters and A2E; and 4) a grouping of points indicating image pixels with shorter fluorescence lifetimes than 730-nm excited synthetic A2E in Fig. 1*C* (*SI Appendix*, Fig. S2*A*). Because image pixels with these shorter fluorescence lifetimes overlapped with 850-nm excited A2E image pixels (Fig. 2*B*) and A2E phasor plots varied with the concentration of A2E (Fig. 1*C*), we attribute these to A2E as well, although they could also indicate presence of other retinal condensation products (30). To assess the relative contributions of A2E and retinyl esters to pixels with mixed composition we followed a method previously described by Ranjit et al. (31) and located their center phasor location halfway between the retinyl esters and A2E phasors, indicating their equal contribution to the decay characteristics. Consequently, Fig. 2*C* and *SI Appendix*, Fig. S2*A* display retinosomes located near RPE cell borders, filling most of the empty spaces visible in the 850-nm FLIM image, and some of the A2E pixels located also near cell borders and pixels with the shorter fluorescence lifetime component were distributed in the interior of the cells (*SI Appendix*, Fig. S2*A*). To compare the content of retinosomes between *Abca4*$^{PV/PV}$*Rdh8*$^{-/-}$ and *Rpe65*$^{-/-}$ mice we selected image pixels that had clusters of phasor points in the same region of the phasor plot in both genotypes (*SI Appendix*, Fig. S2*B*) and created phasor masks (*SI Appendix*, Fig. S2*A*) for ImageJ analyses (*SI Appendix*, Fig. S2*B*). We found that the percentage of the area covered by retinosomes in *Abca4*$^{PV/PV}$*Rdh8*$^{-/-}$ and *Rpe65*$^{-/-}$ mice was 3.7 and 22%, respectively. Considering that retinosomes have an elongated shape along the thickness of the RPE (4, 26), this result is consistent with the higher content of retinyl esters in *Rpe65*$^{-/-}$ mice (*SI Appendix*, Fig. S2*C*). Because some of the pixels displayed characteristics of a mixture of fluorophores, to ascertain the uniformity and distribution of retinosomes and retinal condensation products including A2E along the RPE thickness we collected a series of images along the RPE Z axis and performed phasor FLIM analyses (*SI Appendix*, Fig. S3). We found that retinosomes were located closer to the basal side of the RPE and extended from Z = 0 to Z = 3.5 μm. In contrast, retinal condensation products were located from Z = 1.0 to Z = 5.0 μm, with a maximal presence around Z = 2.5 μm (Movie S1). Moreover, the

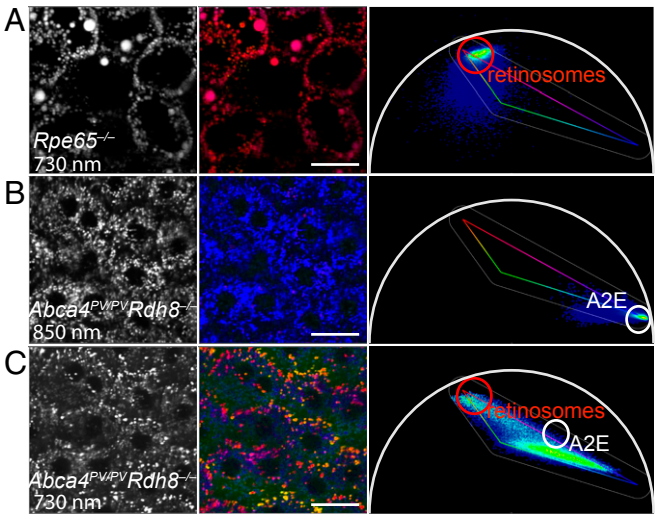

Fig. 2. Distribution of vitamin A metabolites in the intact eye. (*A–C*, *Left*) TPE fluorescence intensity-based images. (*A–C*, *Center*) FLIM phasor images based on colors assigned in semicircle phasor plots presented in *A–C*, *Right*. White circle in phasor plots indicates phasor of synthetic 10 mM A2E, as presented in Fig. 1. (*A*) Data from an albino *Rpe65*$^{-/-}$ mouse obtained with 730-nm excitation. (*B*) Data from an albino 3-mo-old *Abca4*$^{PV/PV}$*Rdh8*$^{-/-}$ mouse obtained with 850-nm excitation. (*C*) Data from the same *Rdh8*$^{-/-}$ *Abca4*$^{PV/PV}$ mouse obtained with 730-nm excitation. (Scale bars, 20 μm.)

majority of the retinosomes displayed some heterogeneity in their fluorescence lifetime distribution, with shorter fluorescence lifetime predominantly around the border of the retinosomes and longer fluorescence lifetime in the center. Thus, overaccumulation of retinal condensation products including A2E does not significantly change the localization of retinyl esters within the RPE.

Spectral Analysis Distinguishes Retinosomes and A2E within RPE Cells without Staining. To compare fluorescence decay and spectral characteristics and to verify conclusions based on the phasor FLIM analyses, we performed spectral phasor analysis (32, 33). We analyzed images of the RPE of *Rdh8*$^{-/-}$*Abca4*$^{PV/PV}$ mice at two excitation wavelengths of 850 nm (Fig. 3*A*) and 730 nm (Fig. 3*B*). Average fluorescence spectra for each excitation wavelength are shown in Fig. 3*C*. At 850-nm excitation wavelength the spectral phasor plot shows a relatively tight phasor cluster which represents all of the pixels from the spectral image. The location of the cluster is like the one obtained for synthetic A2E (Fig. 3 *C*, *Inset*). Slight broadening of the obtained distribution indicates certain fluorescence spectral variation from pixel to pixel. Nevertheless, the average fluorescence spectrum shown in Fig. 3*C* (solid curve) resembles the spectrum obtained for synthetic A2E (Fig. 1*D*). For further analysis, a selection of individual phasors was used to color code pixels within the TPE fluorescence intensity images. Most of the pixels in the image exhibited a fluorescence spectrum very similar to A2E, which is consistent with the results from phasor FLIM analysis.

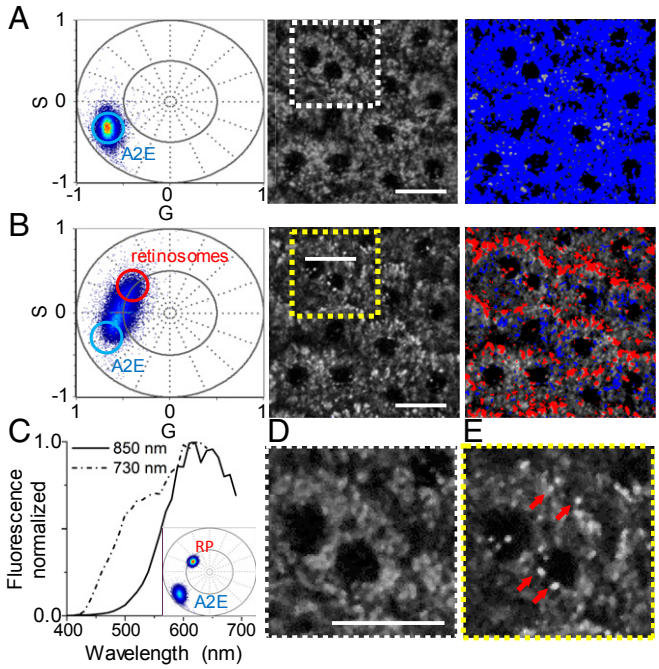

Fig. 3. Spectral analysis distinguishes retinosomes and A2E within RPE cells in albino *Abca4*$^{PV/PV}$*Rdh8*$^{-/-}$ mouse eye without staining. (*A*) Data obtained with 850-nm excitation wavelength. (*B*) Data obtained with 730-nm excitation. (*A* and *B*, *Left*) Spectral phasor plots. (*A* and *B*, *Center*) TPE fluorescence intensity-based images. (*A* and *B*, *Right*) Pseudocolor images obtained by applying the cursor selection in the spectral phasor plots shown in *A* and *B*, *Left*. Dashed-lined squares outline regions presented in higher zoom-in in *D* and *E*. (*C*) Normalized fluorescence emission spectra for 850- and 730-nm excitation from the RPE. (*Inset*) Spectral phasor of pure retinal palmitate and 10 mM A2E in DMSO. RP, retinyl palmitate. (*D*) Zoomed-in image of RPE with 850-nm excitation. (*E*) Zoomed-in image of RPE with 730-nm excitation. Red arrows point to exemplary particles which light up with 730-nm excitation. (Scale bars, 20 μm.)

With 730 nm excitation (Fig. 3 *B*, *Center*), bright particles appear which were not visible with 850 nm excitation. Furthermore, the spectral phasor cloud elongates and shifts toward shorter wavelengths, which is associated with the emergence of a new spectral feature at ∼510 nm (Fig. 3*C*, dashed curve). An ellipsoidal phasor cloud indicates the existence of two spectral components with varying contributions within pixels across the image (34). One end of the ellipsoid clearly matches the spectral phasor signature obtained for retinyl palmitate (Fig. 3 *C*, *Inset*). Two cursors positioned on the distant ends of the phasor cloud show contributions from pure A2E and retinyl esters in the TPE fluorescence image (Fig. 3 *B*, *Right*). Pixels displaying spectral features of retinosomes were color coded in red, while those with A2E-like properties are in blue. Spectral phasor analysis shows that retinosomes are predominantly located near RPE cell borders, filling empty spaces visible in the 850 nm spectral image, and some are near cell nuclei. Fig. 3 *D* and *E* shows zoomed-in images of RPE cell structure in selected regions of interest for 850- and 730-nm excitation, respectively. Spectral phasor analysis is thus consistent with phasor FLIM observations. Furthermore, the appearance of two-photon excited fluorescence from retinosomes at a 730-nm wavelength excitation is not unanticipated, considering that the two-photon excitation spectrum of retinosomes exhibits a maximum at around 730 nm and a steep monotonic decrease when shifting excitation to longer wavelengths, culminating with minimal fluorescence at 850 nm (4, 14). At 730 nm the contribution from pure A2E is largely reduced when compared with 850-nm wavelength excitation. Most of the pixels display mixed fluorescence properties with contributions from both fluorophores. The spectral phasor imaging analysis supports findings from phasor FLIM-based analyses.

Together, these results represent a direct demonstration of the molecular identity of individual granules in the RPE, based on the fluorescence properties of retinoids, namely retinyl esters and retinal condensation products in mouse models (30). Furthermore, this approach does not require the destruction of tissues for immunostaining or for mass spectrometry and high-performance liquid chromatography (HPLC) analyses (11, 14, 35).

Melanin-Related Tissue Alterations Are Mitigated by Imaging with Lower PRF. Because melanin is a significant fluorescent component of the RPE and impacts the maximal permissible exposure limits imposed by American National Standards Institute standards for ocular imaging (36) and affects the mechanisms regulating ocular drug delivery (37), we analyzed its properties under two-photon excitation using cryosections from pigmented mouse models.

First, we investigated the impact of PRF on melanin-mediated retinal tissue alterations during two-photon imaging (Fig. 4). Since melanin can produce transient, brightly luminescent flashes under TPE, to avoid damage to the highly sensitive photon-counting hybrid detector (HyD), we used a photomultiplier tube (PMT) detector for this evaluation. We found that to obtain the same brightness of images quantified as pixel mean gray value (pgv) for 80- and 8-MHz excitation, 45% of the light power that was used for 80-MHz imaging was sufficient to obtain the same brightness with 8-MHz imaging. Furthermore, at light power sufficient to obtain fluorescence images with 80 MHz, brightly luminescent, transient flashes occurred in the choroid and RPE (Fig. 4*B*). With prolonged imaging, bubbles, indicative of tissue alterations, formed in the locations which exhibited a multitude of these flashes and in some of the bubbles, stable fluorescent products accumulated (Fig. 4*C*). These stable fluorescent products did not change over time and were visible even with low laser power of 0.76 mW when using an HyD detector (Fig. 4*D*). Using 8 MHz allowed us to use lower laser power for the same pixel brightness compared to 80 MHz and did not result in bright flashes or tissue alterations, while retaining informative TPE images. Thus 8-MHz PRF enabled imaging with lower laser power than that needed for imaging with 80 MHz.

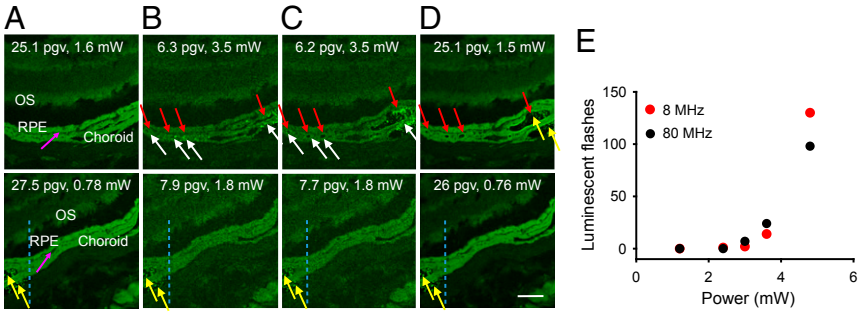

Fig. 4. For the same average laser power, potential for melanin-related laser damage to the retina does not change with PRF. (*A–D*) TPE fluorescence images of retinal cryosections from black *Rpe65*$^{-/-}$ mice obtained consecutively with 750-nm and 80-MHz (*Upper* row) and 8-MHz (*Lower* row) PRF. OS indicates outer segment layer; pink arrows indicate the border between RPE and choroid. Higher average power was needed to obtain images with 80 MHz and results in retina damage, compared to no damage at 8-MHz PRF. Images were obtained with average laser powers that produce approximately the same pixel gray value (pgv); pgv in the RPE and average power are indicated in all images. HyD was used for *A* and *D*; PMT detector was used for *B* and *C*. (*B*) No tissue damage was detected at the beginning of imaging with 3.5-mW laser power. White arrows indicate melanin-related luminescence flashes; red arrows indicate sites where bubbles or tissue damage were evident after 7.2 s exposure, shown in *C*, to 80-MHz 3.5-mW laser light; yellow arrows indicate fluorescent granules formed after exposure to 80-MHz light at 3.5 mW; region to the left of blue dashed lines in images obtained with 8 MHz indicates portion of the sample that was exposed to 80-MHz light. (Scale bar, 50 μm.) (*E*) Quantification of luminescent flashes as a function of laser power at the sample.

However, when we doubled the power to more than was needed for imaging, we also noticed luminescent flashes with 8 MHz. Consequently, we quantified the number of flashes as a function of average light power. We found that for the same average laser power, the number of brightly luminescent flashes induced with 750-nm, 75-fs light pulses in cryosections of the retina from pigmented animals was comparable between 80 and 8 MHz (Fig. 4*E*). Although measurements using cryosections encapsulated between a glass slide and coverslip do not replicate conditions of imaging in vivo, cumulatively, these data indicate that for the same average laser power, the potential for melanin-related laser damage to the retina does not change with PRF.

We next characterized the fluorescence decay and spectral data from the choroid and RPE. To obtain melanin TPE fluorescence lifetime characteristics we acquired data from the retinas of C57BL/6J–*Tyr*$^{c-2J}$/J albino mice and pigmented, C57BL/6J mice excited at 750 nm. We located the melanin phasor by its presence in the choroid of pigmented animals and its absence in albinos (Fig. 5*A*), consistent with a previous report for the TPE of melanin, specifically eumelanin (38). By doing either two- or three-exponent fits of choroidal data we obtained a τ_m of 0.15 ns in wild-type (WT) and *Rpe65*$^{-/-}$ pigmented mice, close to the previously reported value of 0.19 ns for melanocytic nevi (39). Emission spectra from RPE and choroidal melanin showed a broad maximum around 620 nm (Fig. 5*B*), shifted to the blue compared to 640 to 680 nm previously reported for hair eumelanin excited with 1,000-nm, 80-MHz light (38).

Collectively, these important observations constitute a crucial step to future imaging of the pigmented human eye. Reduced PRF enables collection of TPE informative images with reduced average laser power and thus poses substantially less risk for melanin-mediated tissue alterations.

Selection of Optimal Conditions for Imaging the Retina in Pigmented Animals. To obtain maximal imaging contrast from retinosomes, we selected the excitation wavelength by comparing the retinosomes' mean gray pixel value to that of surrounding fluorescent granules as a function of excitation light spectra on retinal sections from the pigmented *Rpe65*$^{-/-}$ mouse eye. Phasor FLIM analysis revealed that most of the RPE pixels contained a mixture of fluorophores including melanin. We identified retinosome pixels based on their phasor signature and measured the fluorescence, along the traces that spanned the choroid and the RPE. We found that the ratio of retinosome fluorescence to that of choroidal melanin was significantly larger for excitation with either 730- or 750-nm light than with 780-nm light (Fig. 5*C*). Furthermore, we verified that FLIM based on phasor analyses does not change with PRF (*SI Appendix*, Fig. S4). Thus, we selected these wavelengths for imaging in living animals. First, we obtained phasor FLIM images from living albino *Rpe65*$^{-/-}$ and *Abca4*$^{PV/PV}$*Rdh8*$^{-/-}$ mice (*SI Appendix*, Fig. S5). Consistent with data presented in Fig. 2, the distribution of pixels in *Rpe65*$^{-/-}$ mice was very tight on the phasor plot; however, it was slightly shifted toward shorter lifetimes, perhaps reflecting a different cellular environment in the living mouse. Because there are no other fluorophores in the RPE of these mice, the data represent the retinosome phasor signature in living *Rpe65*$^{-/-}$ mice. Phasor FLIM data obtained in *Abca4*$^{PV/PV}$*Rdh8*$^{-/-}$ mice with 850-nm excitation displayed tightly distributed pixels on the phasor plot identical to that shown in Fig. 2 for these imaging conditions, indicating that A2E is the source of fluorescence. Imaging *Abca4*$^{PV/PV}$*Rdh8*$^{-/-}$ mice with 750-nm excitation revealed pixels with a mixture of fluorophores, pointing to the possibility of tracking the composition of the RPE fluorophores by their phasor points distributions and FLIM imaging in vivo. Furthermore, by using 750- and/or 730-nm light at reduced PRF it was possible to visualize RPE cell outlines based on the distribution of retinosomes using low laser light exposure. Retinosomes localized close to the cell borders in both black and albino animals (Fig. 6). Moreover, in both types of animals, the brightness, size, and distribution of retinosomes varied somewhat, consistent with those shown in Fig. 2*A*. The retinosomes in the albino mouse could be visualized utilizing 0.17 mW power at 750-nm light, 1-MHz PRF, and a 72-s exposure. Approximately 10 times more energy was needed to obtain informative RPE images in pigmented animals (Fig. 6). Considering that melanin fluorescence lifetime is short, we investigated the possibility of improving RPE image clarity in black animals by either adjusting the focus or gating the fluorescence photons by their arrival time (Fig. 7). To test these possibilities, we obtained FLIM data in black *Rpe65*$^{-/-}$ mice (Fig. 7*A*). The phasor plot revealed that there is a continuum of phasor points along the line in the phasor plot, which means that there is a line of combinations between at least two components that are at the extreme ends of the line (21). Thus, different pixels can have greater or smaller contributions from each of the two components. Considering that no other fluorophores than retinyl esters and melanin are present in the RPE of this genetically modified mouse, we assigned the pure melanin phasor as depicted in Fig. 5*A* and the retinyl ester in *SI Appendix*, Fig. S5. By adjusting the focus 10 μm deeper into the eye we

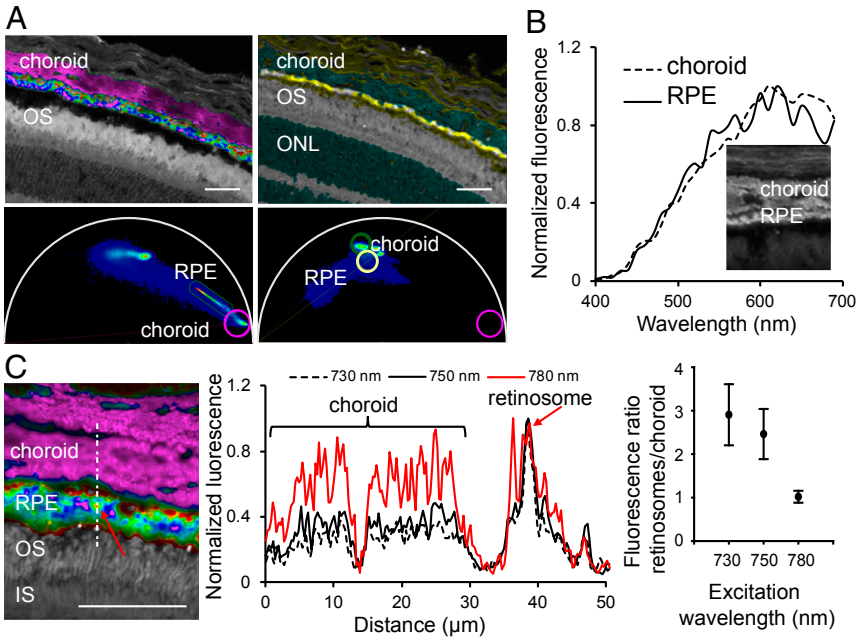

Fig. 5. Selecting optimal wavelength for TPE fluorescence imaging of retinosomes in black animals based on FLIM. (*A*) FLIM images and phasor plots from cryosections of the posterior portion of the eye in 5-mo-old WT black, C57BL/6J and albino, C57BL/6J–Tyr^{c-2J}/J mice. (*A*, *Left*) Data obtained from black mice and (*A*, *Right*) data from albino mice, both with 750-nm excitation. In each phasor plot purple circles indicate location of the melanin phasor or its absence in the albino animal; purple color was selected arbitrarily. In albino mice, phasor points from choroid and outer nuclear layer (ONL) are located in the same region of the semicircle plot and outlined in green. (*B*) TPE fluorescence spectra of RPE and choroid from retinal cryosection of the 3-mo-old black *Rpe65*$^{-/-}$ mouse eye obtained with 850-nm excitation. (*C*, *Left*), TPE FLIM image of the retinal cryosection from 3-mo-old black *Rpe65*$^{-/-}$ mouse. OS, outer segments; IS, inner segments; white dashed line indicates trace along which fluorescence profile shown in the middle was measured; red arrow points to a retinosome. (*C*, *Right*) Ratio of TPE fluorescence from retinosomes to that from choroidal melanin was maximal at 730-nm excitation, closely followed by 750-nm excitation. Data are presented as mean ± SD, $n = 3$. (Scale bars, 40 μm.)

found that there were more blue pixels, indicative of a shorter melanin-like fluorescence lifetime (Fig. 7*A*). To analyze the change in the fraction of the image occupied by the melanin, between the two focal positions, we generated a phasor mask for pixels located in the vicinity of Δ2, exhibiting higher melanin impact on the location of the phasor points in Fig. 7*A*, and applied the ImageJ particle analyze feature, which allows the calculation of the area of the image covered by the object of interest. We calculated that the fraction of RPE area occupied by melanin increased from 8 to 23% in the outlined region of interest. Because these mice do not accumulate A2E in their retina and assuming a diffraction-limited mouse eye point spread function along the eye axis around 8 μm (40), we attribute this shift to the greater contribution of choroidal melanin to the phasor FLIM (Fig. 5). We then tried a gating approach to increase the clarity of imaging retinyl esters by post-processing decay data and rejecting photons with very short arrival times. We found that this method (gating) provided important improvement to the imaging contrast (Fig. 7*B*), such that retinosomes with varying brightness and RPE cells, with an average RPE cell size of 26 μm, in agreement with previous reports (4, 14), could be distinguished. Using the normalized variance as an image metric we determined that filtering out photons with arrival times longer than 0.26 ns did not produce further improvement (Fig. 7*C*).

Analysis of Potential Photodamage Pathways: 1. Free-Electron–Mediated Damage Pathways. The high irradiance values used in nonlinear microscopy enable TPE with IR wavelengths but also pose a risk for photodamage caused by nonlinear photochemistry and the excitation of free electrons into the conduction band (CB) of water from where they can interact with biomolecules and break bonds (41–43). Moreover, solvated electrons have a long lifetime of up to 300 ns during which they can directly interact with biomolecules, and their decay products involve several types of reactive oxygen species (44). In the following, we assessed whether luminescence changes and bubble formation shown in Fig. 4 can be caused by pathways involving the generation of CB electrons ("free" electrons) in water.

Simulation of laser-induced plasma formation is based on the full Keldysh theory of strong-field ionization and a multiple-rate equation (MRE) approach for the description of avalanche ionization (45, 46). The band gap of water is assumed to be $E_{gap} = 9.5$ eV, and a separate initiation channel via solvated electron excitation at an intermediate level $E_{ini} \sim 6.4$ eV is considered (45, 47). At the irradiance levels used in nonlinear microscopy, tunneling plays no role, and strong-field ionization occurs by multiphoton

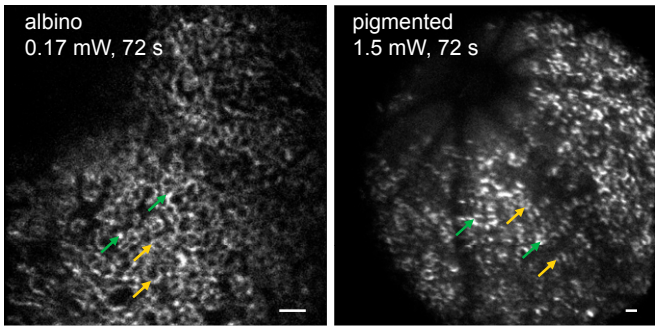

Fig. 6. Imaging of live albino and black mice with low excitation light exposure. *Left* shows RPE in albino and *Right* shows RPE in black *Rpe65*$^{-/-}$, 7-mo-old mice. In both panels, exemplary very bright retinosomes are indicated with green arrows and those less bright with yellow arrows. Excitation at 1-MHz PRF, 0.17 mW of average power, and 72 s imaging time was adequate to visualize cellular details in an albino *Rpe65*$^{-/-}$ mouse. Approximately 10 times more energy was required to image RPE in black animals. (Scale bars, 50 μm.)

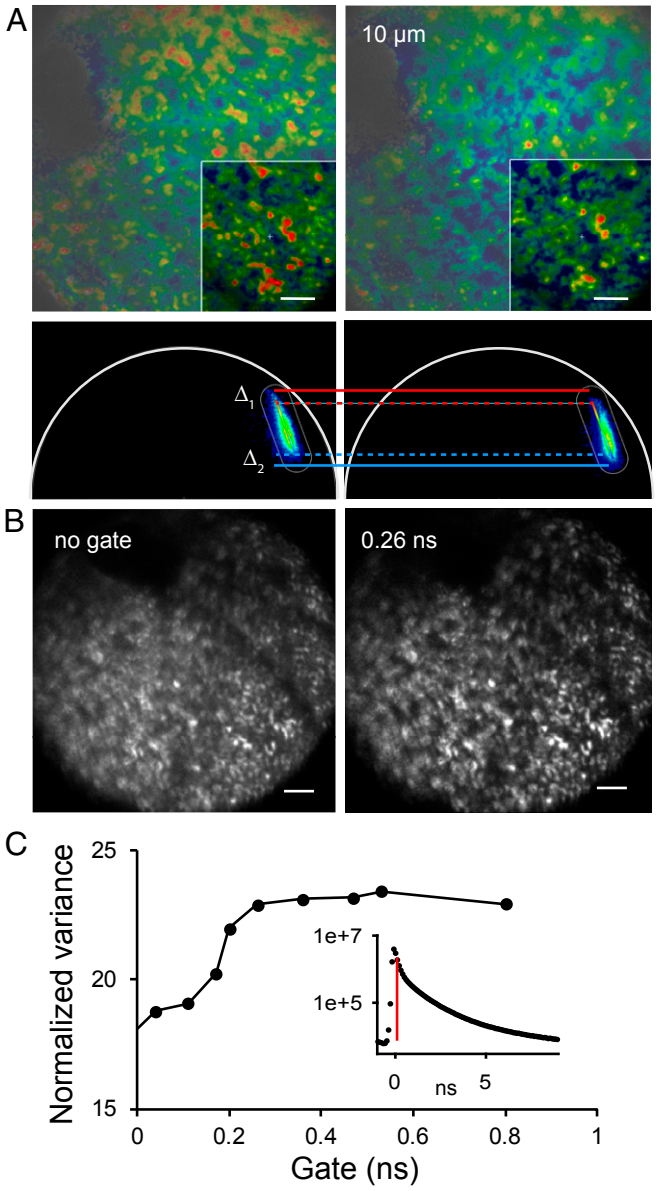

Fig. 7. Overcoming hindrance by melanin in imaging of live pigmented animals by time gating of FLIM. (*A*) FLIM and phasor plots obtained in a live black *Rpe65*$^{-/-}$ mouse. Data on *Right* were obtained at a location 10 μm toward the choroid compared to data on *Left*. Arbitrary colors in FLIM images are based on the colors of the rainbow bar in phasor plots. The same bar was used for both images. Boxed areas in FLIM images represent the areas for which phasor plots are shown. Δ_1 and Δ_2 illustrate shift in decay characteristics toward shorter lifetimes. (*B*) Improvement in image quality obtained with time gating. (*Left*) Intensity-based image using all fluorescence decay data points. (*Right*) Image was composed of data points starting at 0.26 ns after the peak of fluorescence decay for each pixel. Bright spots indicate retinyl ester storage compartments, retinosomes. (*C*) No appreciable improvement in image quality was observed with setting the time gate at 0.26 ns or longer. Fluorescence decay curve for entire image is shown in *Inset*; data points to right of red vertical line, representing position of time gate, were used to form images and quantify image quality using normalized variance. (Scale bars, 100 μm in all images.)

excitation. We considered multiphoton ionization across the entire bandgap and via E_{ini}, followed by up-conversion into the conduction band. The MRE approach is based on a refined impact scheme, which considers the energy levels ($k \times \hbar\omega$) in the conduction band and the electron number density distribution (n_k) in each of these levels (46, 48, 49).

Irradiation parameters used for the simulation were wavelength $\lambda = 750$ nm, pulse duration $\tau_L = 75$ fs (full width at half maximum of a pulse with Gaussian temporal profile), and numerical aperture (NA) = 1.0 (Table 1). The beam quality factor M^2 is assumed to be 1.1. Material parameters for water are effective Drude collision time $\tau_{\text{coll}} = 0.9$ fs and density of preexisting traps, which can host solvated electrons abstracted from excited water molecules, $\chi_{\text{trap}} = 10^{19}$ cm^{-3} (47). The single-pulse energy relates to the average power P_{avg} and PRF by $E_L = P_{\text{avg}}/\text{PRF}$. For a top-hat beam corresponding to an overfilled entrance pupil of the microscope objective, the peak laser irradiance is linked to the single-pulse energy by Eq. **1**,

$$I_0 = \frac{3.73\,E_L}{\tau_L \pi \left(\frac{M^2 d}{2}\right)^2}, \qquad [1]$$

where $d = 1.22\times\lambda/NA$ is the diameter of the central part of the Airy pattern (45). Table 1 summarizes the irradiation parameters employed in the different imaging modalities.

To assess the possibility of plasma-mediated effects, we calculate the free-electron density ρ_e, their average kinetic energy ε_{avg}, and the total number of free electrons produced in the focal volume by one pulse (n_{pulse}) and during the pixel dwell time (n_{total}). The free-electron density corresponding to one electron per plasma volume is $\rho_{1e/\text{Vol}} = 1/V_{\text{plasma}}$ (46). For $\lambda = 750$ nm and NA = 1.0, $\rho_{1e/\text{Vol}} = 7.05 \times 10^{12}$ cm^{-3}. Plasma-mediated damage may arise if the total number of CB electrons produced during the pixel dwell time, n_{total}, is sufficiently large. The severity of the damage depends also on the spectrum of CB electron energies, as more energetic electrons can break stronger bonds or even multiple bonds (41, 50).

SI Appendix, Fig. S6 presents the number density of the free electrons produced by a single laser pulse and their average kinetic energy, ε_{avg}, as a function of peak laser irradiance. We see that for PRF = 80 MHz, the free-electron density is always at least two orders of magnitude smaller than that producing one free electron per pulse in the plasma volume. Since the number of pulses applied during the pixel dwell time of 3.16 μs is 253, plasma-mediated effects can be excluded as a source of photodamage.

For PRF = 8 MHz, the free-electron density becomes significant and at high P_{avg} their energy reaches values of several electron volts that are sufficient to break molecular bonds (51). However, only 25 laser pulses are applied during the pixel dwell time, and the irradiation dose within the focal area A given by $H = E_L \times N_{\text{pulse}}/A = P_{\text{avg}} \times t_{\text{dwell}}/A$ remains below 2 J/cm^2 for all irradiation conditions investigated.

In previous studies on two-photon microscopy of nonpigmented cells and tissues, much higher threshold irradiation doses were reported for the onset of a strong luminescence increase: $H_{\text{th}} = 2.5 \times 10^4$ J/cm^2 at $I_0 = 0.41 \times 10^{12}$ W/cm^2, $\lambda = 730$ nm, $\tau_L = 150$ fs in ref. 52; $H_{\text{th}} = 7.0 \times 10^3$ J/cm^2 at $I_0 = 0.96 \times 10^{12}$ W/cm^2, $\lambda = 730$ nm, $\tau_L = 160$ fs in ref. 53; and $H_{\text{th}} = 1.3 \times 10^3$ J/cm^2 at $I_0 = 4.4 \times 10^{12}$ W/cm^2, $\lambda = 830$ nm, $\tau_L = 130$ fs in ref. 54. The luminescence increase in these studies could have been caused either by nonlinear photochemical changes (55) or by free-electron–mediated effects (41–43). Since the H_{th} values in nonpigmented cells are three to four orders of magnitude higher than the threshold for luminescence onset observed in the present paper within a similar range of irradiances, we can rule out both plasma-mediated effects and nonlinear chemical effects as a primary source of photodamage in pigmented retinal tissue. This conclusion applies for both 80- and 8-MHz PRF and holds even if sequences of several images are recorded. For lower PRFs, the peak irradiance is raised to maintain the same photon yield at constant image acquisition time. According to *SI Appendix*, Fig. S6, this would result in a strong increase of free-electron density with energies sufficiently high to break molecular bonds. However,

Table 1. Irradiation parameters used for two-photon retinal imaging

PRF f_{PRF}, MHz	Avg. power P_{avg}, mW				Single-pulse energy E_L, pJ				Peak irradiance I_0[10^{12} W/cm^2]			
80	1.5	1.6	3.5	4.8	18.75	20.0	43.75	60.0	0.1172	0.125	0.274	0.375
8	0.76	1.8		4.8	95.0	225.0		600	0.594	1.406		3.750

the irradiation dose would likely remain below the threshold for a strong luminescence increase so long as the repetition rates in the megahertz range are employed.

The temperature increase ΔT per laser pulse arising from thermalization of the free-electron energy can be assessed by multiplying the number of free electrons created per focal volume with their average energy, which is given by $E_{gap} + \varepsilon_{avg}$. Cumulative heating is calculated using the modeling tools described in ref. 41 and below. It turns out that the cumulative temperature rise at the end of the pixel dwell time stays below 10^{-2} K even at the highest investigated average power at 8 MHz. Plasma-mediated thermal effects in transparent parts of the retina can thus be excluded, in agreement with the results of previous studies (56).

Analysis of Potential Photodamage Pathways: 2. Thermal Damage Pathways. To assess whether luminescence changes and bubble formation shown in Fig. 4 could be caused by thermal effects, we calculated the change in the temperature, $T(t)$, within laser-irradiated melanosomes after a single 75-fs pulse (λ = 750 nm), during application of a series of 75-fs pulses emitted at 8- and 80-MHz PRF and during continuous-wave (cw) laser irradiation at the same wavelength by solving the differential equation for heat diffusion with the appropriate Green's function, as described in ref. 41. We assumed the temporal shape of the laser pulses to be Gaussian, with half width 75 fs. We used the values ρ_0 = 1,000 kg·m^{-3} for the density, C_p = 4,187 J·K^{-1}·kg^{-1} for the heat capacity, and $\kappa = 1.38 \times 10^{-7}$ m^2·s^{-1} for the heat diffusivity of water. Assuming 70% water content, the respective values for melanosomes are ρ_0 = 1,090 kg·m^{-3} and C_p = 3,300 J·K^{-1}·kg^{-1} (57, 58).

Size and absorption properties of melanin granules were adopted from Williams et al. (59) who investigated the size distribution of melanosomes in mouse retinal pigment epithelium and their spectral absorption. Melanosome sizes in the soma of RPE cells were found to exhibit a broad variation between 100 and 450 nm radius, and the shape varied from approximately round in the soma to ellipsoidal in the apical parts. The absorption coefficient at 532 nm was $\mu_a \sim$ 10,000 cm^{-1}, which can be extrapolated to ~3,000 cm^{-1} at 750 nm using the wavelength scaling of melanin absorption from ref. 57 (https://omlc.org/spectra/melanin/mua.html), $\mu_a \propto \lambda^{-3.48}$.

Simulations were performed for spherical melanin granules of 300 nm radius located at the focus center of the laser beam used for two-photon microscopy. For simplicity, we assume that the granule is located at the focus center during the entire pixel dwell time. While small particles are heated only by the large radiant exposure at the focus center, the average radiant exposure is smaller for large particles as their outer part is irradiated by the small irradiance at the periphery of the focal region. Therefore, the calculation of the temperature rise needs to consider the local radiant exposure as a function of distance r from the optical axis and the path length of each ray traversing the particle that also changes with r. For each r value, the energy absorbed in the melanin granule is calculated based on Lambert–Beer's law, and the total absorbed energy is obtained by integration over all rays in the particle's cross-section. For calculating the heat diffusion into surrounding water, the temperature within the particle is assumed to be homogeneous, corresponding to the total amount of absorbed energy and the thermal properties of the melanosome.

The temperature rise produced by single pulses amounts to ΔT_{pulse} = 45.6 K for an 8-MHz pulse train at P_{avg} = 1.8 mW and to ΔT_{pulse} = 8.9 K for an 80-MHz pulse train at P_{avg} = 3.5 mW. *SI Appendix*, Fig. S7 shows the corresponding $T(t)$ curves for a melanosome with 300 nm radius irradiated by 80- and 8-MHz pulse trains, together with the temperature evolution for cw irradiation with the same average power. $T(t)$ curves are normalized to the temperature jump ΔT_{pulse} produced by a single pulse and show the heat accumulations during a pulse train.

The $T(t)$ curves exhibit a steep temperature rise (ΔT_{pulse}) during each laser pulse, followed by a drop between pulses due to heat diffusion out of the focal volume. While ΔT_{pulse} remains the same during the entire pulse train, heat diffusion increases with increasing focal temperature until the cw component of the temperature reaches a saturation value. For a given average power, the saturation value of the cw component of $T(t)$ is always the same, regardless of pulse repetition rate. This holds although the temperature rise ΔT_{pulse} by individual pulses is much larger at 8 MHz because the heat accumulation factor (HAF) = $T_{max,cumul}/\Delta T_{pulse}$ is smaller at the lower repetition rate. While HAF was 11.48 for the 80-MHz pulse train, it was only 1.75 at 8 MHz. The difference is even larger for the heat accumulation factors of the cw component, where the values are 10.9 and 1.09, respectively.

A reduction of the pulse repetition frequency below 8 MHz at constant photon yield will reduce the HAF only slightly as it is already small at 8 MHz, but it will result in a significant increase of temperature rise by individual pulses, which increases the risk of thermomechanical damage.

Two-photon imaging at lower pulse repetition rates can be performed at lower average power because of the quadratic dependence of fluorescent photon yield on irradiance (or pulse light intensity, respectively) (15, 16). Specifically, $P_{avg} \leq$ 1.8 mW was sufficient to record images at 8 MHz, whereas up to 3.5 mW was needed at 80 MHz. *SI Appendix*, Table S1 summarizes the simulation results for the temperature evolution and maximum temperature at different pulse repetition frequencies for melanosomes of R_m = 300 nm. Outside the melanosomes, the temperature drops rapidly due to heat diffusion but is significantly elevated in a shell that extends approximately up to twice the particle's radius (41). We conclude that photodamage in retinal imaging occurs through thermally mediated pathways, whereas plasma-mediated effects play no role.

Together, these technical applications and their optimization and the resulting data suggest a possibility of safe imaging the human retina and RPE with precise identification and localization of retinal fluorophores.

Discussion

Ophthalmic imaging techniques are cornerstones in retinal disease management and the identification of new treatments. Despite tremendous progress, current methods for retinal imaging such as color photography, narrow band reflectance photography, and OCT provide structural and in the case of OCT volumetric data while differentiating layers of specialized cells in the retina; however, they reveal tissue dysfunction only when a structural phenotype already exists and, therefore, they are insensitive to early stages of disease. Furthermore, fundus autofluorescence provides some information about retinal condensation products, but retinyl esters are undetectable using this method. Thus, imaging that can access a different aspect of tissue function, encoded at the biochemical level through intrinsically fluorescent metabolites fundamental to visual

processing, offers the possibility of identifying a unique series of disease-specific early biomarkers. Previously, through TPE imaging studies combined with HPLC and mass spectrometry methods using WT and retinal disease mouse models, retinosomes and their role in the retinoid cycle were discovered (7, 60). Also, by tuning excitation spectra and applying spectral detection, the overaccumulation of A2E in the RPE of mouse models of light-induced retinal degeneration was discerned (4). Moreover, TPE-based images showing the three-dimensional arrangement of retinal photoreceptors and the RPE revealed the sequence of events leading to retina degeneration following bright light illumination and the effect of drugs on preventing it (10, 11). While there is increasing interest in applying FLIM to the early detection of retinal diseases in humans (23), retinyl esters cannot be detected with existing one-photon modalities. Previous methods based on artificial dyes do not provide information about retinal metabolites (61). Furthermore, noninvasive identification of retinal fluorophores without the need for tissue destruction is missing. Although it was possible to image the retina in albino animals with exposure levels equivalent to the safe imaging of the human eye, imaging of pigmented animals required exposures above safety limits (40). In research reported here, we present low-level exposure two-photon retinal imaging data from albino and pigmented animals attained by controlling temporal properties of a pulsing laser light. Furthermore, lower exposures permitted imaging of pigmented animals without damaging the retina, yet enabled the molecular identification of endogenous fluorophores in tissues by utilizing fluorescence decay and spectral data.

Reducing PRF increased TPE efficiency, resulting in higher fluorescence for the same average power (Fig. 1 and *SI Appendix*, Fig. S1) (15), thus allowing the collection of informative images with less laser light exposure (Fig. 4). For A2E we observed more than a 10-fold fluorescence increase between 8 and 80 MHz (Fig. 1*B*). However, for retinyl palmitate the increase was smaller for higher excitation powers. Possible explanations might include fluorophore saturation and the counting rate limit of the detector considering the high transient photon flux from retinyl palmitate (*SI Appendix*, Fig. S1) (62, 63).

The quantification and mapping of the distribution of granules with diverse molecular composition (Fig. 2 and *SI Appendix*, Fig. S2) were demonstrated noninvasively, based on differences in fluorescence decay and spectral characteristics of A2E and retinyl esters. Additionally, phasors of synthetic compounds differed from the results obtained in intact eyes (Fig. 2 and *SI Appendix*, Fig. S5). These differences can be attributed to the molecular environments (64) and the fluorescence decay dependence on concentration (Fig. 1*C*). Furthermore, the smaller NA of the mouse eye compared to the microscope objective results in a larger focal volume and the concomitant contribution of signals from neighboring areas. Whereas the 850-nm FLIM data derived from the $Abca4^{PV/PV}Rdh8^{-/-}$ mouse RPE closely resembled those of a synthetic A2E solution (Fig. 1*C*), 730-nm excitation revealed a multitude of granules including retinosomes, A2E at various concentrations, other retinal condensation products, and granules that exhibited mixed properties (Fig. 2 and *SI Appendix*, Fig. S2).

Based on the data in *SI Appendix*, Table S1, we can identify three possible thermally mediated damage pathways: 1) Thermoelastic stress arising from impulsive heating may induce cavitation and melanosome fragmentation. 2) Vaporization into the bubble nuclei produced by cavitation will lead to bubble growth, when the focal temperature exceeds the boiling point (100 °C). And 3) temperature-dependent chemical changes of biomolecules may change their structural and optical properties.

Unlike the thermomechanical changes occurring in the first and second photodamage pathways that are characterized by well-defined temperature thresholds, the thermochemical changes are rate processes that depend both on temperature and on time. In the following, we discuss all three pathways step by step and analyze their possible contribution to the damage patterns observed for different pulse repetition rates (Fig. 4).

Thermoelastic Stress. The heating by a 75-fs pulse occurs by vibrational relaxation of excited states in the melanin granule, which is completed within a few picoseconds. This is much faster than thermal expansion of the granule, because a thermal expansion wave propagates with sound velocity c_s, and thermal expansion is completed when the expansion wave has traveled through the absorber with diameter $2 \times R_m$. For a particle with a 300-nm radius, $2 \times R_m/c_s = 600$ nm/1,480 m/s = 0.405 ns, which is much longer than the heating time. As a consequence, energy deposition is isochoric, and compressive thermoelastic stress builds up during heating (41, 65, 66). The pressure amplitude produced by a given temperature rise increases with increasing ambient temperature because the Grüneisen coefficient, which relates ΔT_{pulse} to Δp, increases with T (67). After the deposition of "stress confined" energy into an absorber of finite size, it expands, and then a relaxation stress wave is emitted. This stress wave is bipolar; i.e., the compressive part is followed by a tensile part, when the material that was accelerated during thermal expansion comes to a halt. The tensile wave propagates from the outer boundary of the particle toward its center, whereby it is focused. For a spherical, homogeneously absorbing particle, the tensile stress in the particle's center is 16 times as large as the uniformly distributed initial compressive stress (65). The material will rupture and a cavitation bubble will form, when a trajectory in the (p/T) phase diagram crosses the kinetic spinodal ("superheat") limit (41, 66). For spherical absorbers this occurs even when the peak temperature stays well below the boiling point (65). When melanosomes are impulsively heated, the tensile stress can fracture the particle (68, 69). This will expose the bubble nucleus to surrounding tissue water and lower the nucleation threshold below the value observed under non–stress-confined conditions (irradiation with nanosecond pulses), for which values of 112 °C (58) and 136 °C (70) have been reported.

While for 80-MHz pulse repetition frequency the lowering of the bubble nucleation threshold seems to be the main thermoelastic effect, the larger temperature jumps during an 8-MHz pulse train can induce oscillating cavitation bubbles (41) and will have a larger fragmentation yield (68). Lowering the PRF below 8 MHz will further increase the fragmentation yield.

Vapor Bubble Growth. A bubble nucleus will grow by vaporization of surrounding water, if the temperature-dependent vapor pressure exceeds the outer pressure, which is given by the sum of hydrostatic pressure and Laplace pressure $p_\gamma = 2\gamma/R$ caused by surface tension, with coefficient $\gamma = 0.073$ N/m at room temperature, and $\gamma = 0.059$ N/m at 100 °C. For large bubbles, where surface tension can be neglected, a bubble can grow once $T >$ 100 °C, but a larger temperature is required for small bubbles. More specifically, for a bubble of, e.g., 1-μm radius, $p_\gamma = 0.118$ MPa at 100 °C. Considering the temperature dependence of surface tension, T must be larger than 120 °C to allow bubble growth (71). Thus, a vapor bubble can form if the sum of room temperature and cumulative laser-induced temperature rise exceeds 120 °C. With the imaging parameters of Fig. 4, this condition is approximately fulfilled for a melanosome of 300 nm radius at 80-MHz pulse repetition frequency at $P_{avg} = 3.5$ mW, but the temperature produced by the 8-MHz pulse train at $P_{avg} = 1.8$ mW stays below the limit. When a further PRF reduction goes along with a further lowering of average power, vapor bubble growth can be avoided even more effectively.

Thermochemical Changes. Heating of proteins to temperatures well above 100 °C can induce an increase of fluorescence, similar to that observed at tissue surfaces after femtosecond laser ablation (72, 73). Qin et al. (73) observed a strong fluorescence

increase in various types of tissues, albumin, and lysin heated to 200 °C for 15 min. We hypothesize that similar thermochemical changes are responsible for the fluorescence increase in the immediate vicinity of the melanosomes observed after imaging with 3.5 mW average power at 80 MHz (Fig. 4). This interpretation will need further substantiation in the future because the pixel dwell time is much shorter than the heat exposure time in ref. 73, and it is known that thermal denaturation thresholds increase with decreasing heat exposure time (74). However, it may well be that the photodamage kinetics of a femtosecond pulse series exhibit synergies between thermochemical changes and nonlinear photochemical effects that are neither observed in short-time cw exposures nor observed after femtosecond laser irradiation of tissues at room temperature.

Since the total yield of thermally changed molecules depends not just on peak temperature but also on heat exposure time, 80-MHz trains of 3.5 mW average power will produce more alterations than 8-MHz pulse trains with $P_{avg} = 1.8$ mW because their cw component is almost twice as high. However, once fluorescence changes have been produced by an 80-MHz pulse train, they are long lasting and fluorescence can be excited also by low-power 8-MHz pulse series, as seen in Fig. 4 *A*, *Lower*. Thus, melanin-related thermochemically induced damage of the retinal pigment epithelium as well as vapor bubble growth can be mitigated by a reduction of pulse repetition frequency from 80 to 8 MHz, due to the lower average power providing the same fluorescence photon yield. This result is in agreement with previous findings on multiphoton microscopy of pigmented skin (16). It is conceivable that lowering the PRF below 8 MHz may be beneficial, but it will increase the fragmentation yield of the melanin granules. Thus, further investigations for identifying the optimum PRF are still warranted to identify the optimum PRF that may lie below 8 MHz.

Thus, analysis of the possible damage pathways, including free-electron–mediated damage, revealed that thermally produced changes originating from laser-induced heating of the melanin granules are the main cause of the observed alterations and that imaging with reduced PRF is mitigating these changes. The irradiation dose applied during the recording of individual images is too small to induce a significant amount of photoproducts by nonlinear photochemistry of plasma-mediated effects.

By analyzing the spectral and decay properties of melanin and pigmented tissue alterations under TPE and reviewing the potential for tissue damage by individual or a series of femtosecond pulses, we optimized excitation wavelength, time gating of fluorescence photons, and PRF to obtain informative images using noninvasive imaging conditions (41, 45, 46), critical for translating these findings to applications in humans.

In conclusion, we noninvasively determined the composition of individual granules in the RPE and determined the relative content of vitamin A stores containing retinyl esters and deposits of retinoid cycle byproducts by their fluorescence decay and spectral characteristics. Furthermore, we have shown that risk for eye tissue alteration by TPE imaging is mitigated with reduced PRF.

Methods

Animals and Study Approval. All mice were housed in the animal facility in the University of California, Irvine Laboratory Animal Resources (ULAR) center, where they were maintained on a normal mouse chow diet under complete darkness or in a 12-h light (~10 lx)/12-h dark cyclic environment. Mice were anesthetized with an i.p. injection of ketamine (20 mg/mL) and xylazine (2 mg/mL) diluted with water at a dose of 5 μL/g body weight. Before imaging, mouse pupils were dilated with 1% tropicamide. Animal procedures were approved by the Animal Care Committees at the University of California, Irvine (UCI) and conformed to the recommendations of both the American Veterinary Medical Association Panel on Euthanasia and the Association for Research in Vision and Ophthalmology under assurance no. A-3416-01. WT, black C57BL/6J mice and albino C57BL/6J–Tyr^{c-2J}/J mice were obtained from The Jackson Laboratories. Albino and black $Rpe65^{-/-}$ mice were generated as previously described (4, 75). Albino $Abca4^{PV/PV}Rdh8^{-/-}$ mice were obtained by cross-breeding of previously described albino $Abca4^{PV/PV}$ (12) with albino $Rdh8^{-/-}$ mice (76). PCR was performed to select animals with genotypes which were homozygous.

TPE Imaging with Reduced PRF. To increase the TPE fluorescence and minimize laser light exposure needed to obtain informative images of the retina, our custom TP imaging system was redesigned to include a new light source delivering laser pulses with controlled and adjustable PRF, based on the inverse relationship between TP absorption rate and PRF for the same average power (Fig. 1) (14–16). Reducing the PRF was achieved with the Conoptics pulse selection system composed of an electro-optic modulator, indicated in Fig. 1*A* as pulse picker; a countdown module, counter in Fig. 1*A*; and a power supply. Synchronization outputs from the lasers provided an electrical reference pulse train for the counter, which in turn sent the signal to the pulse picker power supply unit. Pulse picker is a transverse field-type Pockels cell, which changes the state of polarization of the input light according to the control voltage. Control voltage is adjusted in such a way that in a low state all of the light goes through the modulator and analyzer, whereas in a high state all of the light is blocked. The desired PRF is attained by selecting the number of pulses to be rejected, *n*, by the pulse picker using the counter; e.g., for $n = 9$ every 10th pulse is transmitted, resulting in a PRF = 80 MHz/10 = 8 MHz. Monitoring the PRF and relative amplitude of the laser pulses was enabled by connecting the output from the photodiode (PD) to an oscilloscope. Thus, it was possible to obtain controlled average power measurements at the imaging plane, for the known amplitude of laser pulses. Optimal alignment of the pulse picker electro-optic modulator (Fig. 1) was achieved by first adjusting the position of the input and output windows so there was no detectable diffraction or beam clipping and then by physically rotating it to maximize passive light transmission through the internal polarizer. Before each data collection series at a specified PRF and wavelength, the bias voltage on the pulse picker power supply unit was adjusted to maximize the amplitude of the selected pulses and minimize the amplitude of the unwanted pulses and dispersion precompensation was adjusted to account for the Pockels cell.

FLIM. To obtain FLIM data we used a modified Leica TCS SP8 microscope with Falcon architecture (77) shown in Fig. 1 and described in detail in *SI Appendix, Methods*.

Hyperspectral Imaging. Spectral data were obtained using a modified Leica TCS SP8 with an integrated spectral detection. In this approach spectral components of the fluorescent light were separated spatially by the prism, isolated by a motorized slit, and detected by an HyD in a descanned configuration. For each pixel within the image, its fluorescence emission spectrum was recorded and separated in up to 30 wavelength channels, from 400 to 700 nm. The acquisition time for one dataset was ~39 s, 1.3 s per single-wavelength channel.

The raw data obtained from the microscope software were analyzed in the Globals for Images: SimFCS 4 software package using a spectral phasor approach, as previously described (33, 78). The fluorescence spectrum of each pixel was transformed into a spectral phasor plot using (33)

$$\text{x coordinate} = G = \frac{\sum_\lambda I(\lambda)\cdot\cos(2\pi\lambda/L)}{\sum_\lambda I(\lambda)},$$
$$\text{and} \qquad [2]$$
$$\text{y coordinate} = S = \frac{\sum_\lambda I(\lambda)\times\sin(2\pi\lambda/L)}{\sum_\lambda I(\lambda)},$$

where $I(\lambda)$ is the fluorescence intensity at each wavelength channel of the spectrum and L is the total wavelength range. The x and y coordinates have values from −1 to 1 and are plotted in a scatter plot called a spectral phasor plot. The position of each data point in the plot is simultaneously related to the center of mass of the spectrum and its full width at half-maximum (FWHM). Therefore, pixels with similar spectral properties will form clouds of points located in close proximity. The angular position of each point is related to the center of mass of the spectrum, while radial position is related to its FHWM. The spectral phasor approach enables quick identification of emission spectra of pixels within the image. Various pixels of interest can be selected with a cursor and color coded in the TPE fluorescence image, to highlight pixels with various spectral features.

Statistics. Data from at least three independent experiments were presented as means ± SD.

Data Availability. All data supporting the findings of this study are available within this paper and *SI Appendix*.

ACKNOWLEDGMENTS. We thank Dr. T. Michael Redmond (NIH) for *Rpe65*$^{-/-}$ mice. We also thank Drs. Andrew Browne and Katarzyna Komar for stimulating discussions. This research was supported in part by grants from the NIH to K.P. (EY009339, EY027283, EY025451). We also acknowledge an unrestricted grant from Research to Prevent Blindness to the Department of Ophthalmology, University of California, Irvine. X.-X.L. and A.V. were supported by the Air Force Office of Scientific Research Grant FA9550-18-1-0521. M.W. acknowledges the European Union's Horizon 2020 research and innovation program Grant 666295 and Project TEAM TECH/2016-3/20 carried out within the TEAM-TECH program of the Foundation for Polish Science cofinanced by the European Union under the European Regional Development Fund.

1. D. Huang *et al*., Optical coherence tomography. *Science* **254**, 1178–1181 (1991).
2. S. A. Burns, A. E. Elsner, K. A. Sapoznik, R. L. Warner, T. J. Gast, Adaptive optics imaging of the human retina. *Prog. Retin. Eye Res.* **68**, 1–30 (2019).
3. S. Schmitz-Valckenberg, F. G. Holz, A. C. Bird, R. F. Spaide, Fundus autofluorescence imaging: Review and perspectives. *Retina* **28**, 385–409 (2008).
4. G. Palczewska *et al*., Noninvasive multiphoton fluorescence microscopy resolves retinol and retinal condensation products in mouse eyes. *Nat. Med.* **16**, 1444–1449 (2010).
5. E. A. Boettner, J. R. Wolter, Transmission of the ocular media. *Invest. Ophthalmol.* **1**, 776–783 (1962).
6. R. Kian, S. M. S. Ahmadian, M. S. Zakerhamidi, Photo-physical properties of different types of vitamin A in solvent media. *J. Mol. Struct.* **1080**, 8–13 (2015).
7. Y. Imanishi, M. L. Batten, D. W. Piston, W. Baehr, K. Palczewski, Noninvasive two-photon imaging reveals retinyl ester storage structures in the eye. *J. Cell Biol.* **164**, 373–383 (2004).
8. M. L. Batten *et al*., Lecithin-retinol acyltransferase is essential for accumulation of all-trans-retinyl esters in the eye and in the liver. *J. Biol. Chem.* **279**, 10422–10432 (2004).
9. M. L. Batten *et al*., Pharmacological and rAAV gene therapy rescue of visual functions in a blind mouse model of Leber congenital amaurosis. *PLoS Med.* **2**, e333 (2005).
10. G. Palczewska *et al*., Noninvasive two-photon microscopy imaging of mouse retina and retinal pigment epithelium through the pupil of the eye. *Nat. Med.* **20**, 785–789 (2014).
11. A. Maeda *et al*., Two-photon microscopy reveals early rod photoreceptor cell damage in light-exposed mutant mice. *Proc. Natl. Acad. Sci. U.S.A.* **111**, E1428–E1437 (2014).
12. N. Zhang *et al*., Protein misfolding and the pathogenesis of ABCA4-associated retinal degenerations. *Hum. Mol. Genet.* **24**, 3220–3237 (2015).
13. P. D. Kiser, K. Palczewski, Retinoids and retinal diseases. *Annu. Rev. Vis. Sci.* **2**, 197–234 (2016).
14. G. Palczewska *et al*., Two-photon imaging of the mammalian retina with ultrafast pulsing laser. *JCI Insight* **3**, e121555 (2018).
15. W. Denk, J. H. Strickler, W. W. Webb, Two-photon laser scanning fluorescence microscopy. *Science* **248**, 73–76 (1990).
16. B. R. Masters *et al*., Mitigating thermal mechanical damage potential during two-photon dermal imaging. *J. Biomed. Opt.* **9**, 1265–1270 (2004).
17. M. A. Albota, C. Xu, W. W. Webb, Two-photon fluorescence excitation cross sections of biomolecular probes from 690 to 960 nm. *Appl. Opt.* **37**, 7352–7356 (1998).
18. F. Helmchen, W. Denk, Deep tissue two-photon microscopy. *Nat. Methods* **2**, 932–940 (2005).
19. A. Konar, J. D. Shah, V. V. Lozovoy, M. Dantus, Optical response of fluorescent molecules studied by synthetic femtosecond laser pulses. *J. Phys. Chem. Lett.* **3**, 1329–1335 (2012).
20. S. Pang, A. T. Yeh, C. Wang, K. E. Meissner, Beyond the 1/Tp limit: Two-photon-excited fluorescence using pulses as short as sub-10-fs. *J. Biomed. Opt.* **14**, 054041 (2009).
21. S. Ranjit, L. Malacrida, D. M. Jameson, E. Gratton, Fit-free analysis of fluorescence lifetime imaging data using the phasor approach. *Nat. Protoc.* **13**, 1979–2004 (2018).
22. M. Y. Berezin, S. Achilefu, Fluorescence lifetime measurements and biological imaging. *Chem. Rev.* **110**, 2641–2684 (2010).
23. C. Dysli *et al*., Fluorescence lifetime imaging ophthalmoscopy. *Prog. Retin. Eye Res.* **60**, 120–143 (2017).
24. D. Schweitzer *et al*., Towards metabolic mapping of the human retina. *Microsc. Res. Tech.* **70**, 410–419 (2007).
25. G. A. Murashova *et al*., Multimodal nonlinear optical imaging of unstained retinas in the epi-direction with a sub-40 fs Yb-fiber laser. *Biomed. Opt. Express* **8**, 5228–5242 (2017).
26. T. M. Redmond *et al*., Rpe65 is necessary for production of 11-cis-vitamin A in the retinal visual cycle. *Nat. Genet.* **20**, 344–351 (1998).
27. M. L. Katz, T. M. Redmond, Effect of Rpe65 knockout on accumulation of lipofuscin fluorophores in the retinal pigment epithelium. *Invest. Ophthalmol. Vis. Sci.* **42**, 3023–3030 (2001).
28. J. R. Sparrow, M. Boulton, RPE lipofuscin and its role in retinal pathobiology. *Exp. Eye Res.* **80**, 595–606 (2005).
29. T. L. Lenis *et al*., Expression of ABCA4 in the retinal pigment epithelium and its implications for Stargardt macular degeneration. *Proc. Natl. Acad. Sci. U.S.A.* **115**, E11120–E11127 (2018).
30. J. R. Sparrow, Y. Wu, C. Y. Kim, J. Zhou, Phospholipid meets all-trans-retinal: The making of RPE bisretinoids. *J. Lipid Res.* **51**, 247–261 (2010).
31. S. Ranjit, R. Datta, A. Dvornikov, E. Gratton, Multicomponent analysis of phasor plot in a single pixel to calculate changes of metabolic trajectory in biological systems. *J. Phys. Chem. A* **123**, 9865–9873 (2019).
32. F. Fereidouni, A. N. Bader, H. C. Gerritsen, Spectral phasor analysis allows rapid and reliable unmixing of fluorescence microscopy spectral images. *Opt. Express* **20**, 12729–12741 (2012).
33. O. Golfetto, E. Hinde, E. Gratton, The Laurdan spectral phasor method to explore membrane micro-heterogeneity and lipid domains in live cells. *Methods Mol. Biol.* **1232**, 273–290 (2015).
34. F. Fereidouni, A. N. Bader, A. Colonna, H. C. Gerritsen, Phasor analysis of multiphoton spectral images distinguishes autofluorescence components of in vivo human skin. *J. Biophotonics* **7**, 589–596 (2014).
35. G. Palczewska, M. Golczak, D. R. Williams, J. J. Hunter, K. Palczewski, Endogenous fluorophores enable two-photon imaging of the primate eye. *Invest. Ophthalmol. Vis. Sci.* **55**, 4438–4447 (2014).
36. F. C. Delori, R. H. Webb, D. H. Sliney; American National Standards Institute, Maximum permissible exposures for ocular safety (ANSI 2000), with emphasis on ophthalmic devices. *J. Opt. Soc. Am. A Opt. Image Sci. Vis.* **24**, 1250–1265 (2007).
37. A. K. Rimpelä *et al*., Implications of melanin binding in ocular drug delivery. *Adv. Drug Deliv. Rev.* **126**, 23–43 (2018).
38. T. B. Krasieva *et al*., Two-photon excited fluorescence lifetime imaging and spectroscopy of melanins in vitro and in vivo. *J. Biomed. Opt.* **18**, 31107 (2013).
39. E. Dimitrow *et al*., Spectral fluorescence lifetime detection and selective melanin imaging by multiphoton laser tomography for melanoma diagnosis. *Exp. Dermatol.* **18**, 509–515 (2009).
40. D. J. Wahl, M. J. Ju, Y. Jian, M. V. Sarunic, Non-invasive cellular-resolution retinal imaging with two-photon excited fluorescence. *Biomed. Opt. Express* **10**, 4859–4873 (2019).
41. A. Vogel, J. Noack, G. Huttman, G. Paltauf, Mechanisms of femtosecond laser nanosurgery of cells and tissues. *Appl. Phys. B* **81**, 1015–1047 (2005).
42. A. A. Voronin, A. M. Zheltikov, Ionization penalty in nonlinear optical bioimaging. *Phys. Rev. E Stat. Nonlin. Soft Matter Phys.* **81**, 051918 (2010).
43. D. Débarre, N. Olivier, W. Supatto, E. Beaurepaire, Mitigating phototoxicity during multiphoton microscopy of live Drosophila embryos in the 1.0-1.2 μm wavelength range. *PLoS One* **9**, e104250 (2014).
44. D. N. Nikogosyan, A. A. Oraevsky, V. I. Rupasov, 2-Photon ionization and dissociation of liquid water by powerful laser Uv-radiation. *Chem. Phys.* **77**, 131–143 (1983).
45. N. Linz, S. Freidank, X. X. Liang, A. Vogel, Wavelength dependence of femtosecond laser-induced breakdown in water and implications for laser surgery. *Phys. Rev. B* **94**, 024113 (2016).
46. X. X. Liang, Z. Zhang, A. Vogel, Multi-rate-equation modeling of the energy spectrum of laser-induced conduction band electrons in water. *Opt. Express* **27**, 4672–4693 (2019).
47. N. Linz *et al*., Wavelength dependence of nanosecond infrared laser-induced breakdown in water: Evidence for multiphoton initiation via an intermediate state. *Phys. Rev. B* **91**, 134114 (2015).
48. B. H. Christensen, P. Balling, Modeling ultrashort-pulse laser ablation of dielectric materials. *Phys. Rev. B* **79**, 155424 (2009).
49. B. Rethfeld, Unified model for the free-electron avalanche in laser-irradiated dielectrics. *Phys. Rev. Lett.* **92**, 187401 (2004). Correction in: *Phys. Rev. Lett.* **92**, 209901 (2004).
50. G. Aad *et al*.; ATLAS Collaboration, Observation of light-by-light scattering in ultraperipheral Pb+Pb collisions with the ATLAS detector. *Phys. Rev. Lett.* **123**, 052001 (2019).
51. Y. Zheng, L. Sanche, Effective and absolute cross sections for low-energy (1-30 eV) electron interactions with condensed biomolecules. *Appl. Phys. Rev.* **5**, 021302 (2018).
52. K. König, P. T. So, W. W. Mantulin, B. J. Tromberg, E. Gratton, Two-photon excited lifetime imaging of autofluorescence in cells during UVA and NIR photostress. *J. Microsc.* **183**, 197–204 (1996).
53. R. Orzekowsky-Schroeder *et al*., In vivo spectral imaging of different cell types in the small intestine by two-photon excited autofluorescence. *J. Biomed. Opt.* **16**, 116025 (2011).
54. W. Supatto, D. Débarre, E. Farge, E. Beaurepaire, Femtosecond pulse-induced microprocessing of live Drosophila embryos. *Med. Laser Appl.* **20**, 207–216 (2005).
55. K. Koening, *Handbook of Biological Confocal Microscopy*, (Springer, New York, ed. 3, 2006).
56. A. Schönle, S. W. Hell, Heating by absorption in the focus of an objective lens. *Opt. Lett.* **23**, 325–327 (1998).
57. S. L. Jacques, R. D. Glickman, J. A. Schwartz, "Internal absorption coefficient and threshold for pulsed laser disruption of melanosomes isolated from retinal pigment epithelium". *Laser-Tissue Interaction VII, Proceedings of SPIE*, 468–477 (1996).
58. S. L. Jacques, D. J. McAuliffe, The melanosome: Threshold temperature for explosive vaporization and internal absorption coefficient during pulsed laser irradiation. *Photochem. Photobiol.* **53**, 769–775 (1991).
59. M. A. Williams, L. H. Pinto, J. Gherson, The retinal pigment epithelium of wild type (C57BL/6J +/+) and pearl mutant (C57BL/6J pe/pe) mice. *Invest. Ophthalmol. Vis. Sci.* **26**, 657–669 (1985).
60. Y. Imanishi, V. Gerke, K. Palczewski, Retinosomes: New insights into intracellular managing of hydrophobic substances in lipid bodies. *J. Cell Biol.* **166**, 447–453 (2004).

61. J. A. Feeks, J. J. Hunter, Adaptive optics two-photon excited fluorescence lifetime imaging ophthalmoscopy of exogenous fluorophores in mice. *Biomed. Opt. Express* **8**, 2483–2495 (2017).
62. R. Heintzmann, T. M. Jovin, C. Cremer, Saturated patterned excitation microscopy–A concept for optical resolution improvement. *J. Opt. Soc. Am. A Opt. Image Sci. Vis.* **19**, 1599–1609 (2002).
63. A. Diaspro, G. Chirico, M. Collini, Two-photon fluorescence excitation and related techniques in biological microscopy. *Q. Rev. Biophys.* **38**, 97–166 (2005).
64. J. R. Lakowicz, H. Szmacinski, K. Nowaczyk, M. L. Johnson, Fluorescence lifetime imaging of free and protein-bound NADH. *Proc. Natl. Acad. Sci. U.S.A.* **89**, 1271–1275 (1992).
65. G. Paltauf, H. Schmidt-Kloiber, Photoacoustic cavitation in spherical and cylindrical absorbers. *Appl. Phys. A* **68**, 525–531 (1999).
66. A. Vogel, V. Venugopalan, Mechanisms of pulsed laser ablation of biological tissues. *Chem. Rev.* **103**, 577–644 (2003). Correction in: *Chem. Rev.* **103**, 2079 (2003).
67. M. Pramanik, L. V. Wang, Thermoacoustic and photoacoustic sensing of temperature. *J. Biomed. Opt.* **14**, 054024 (2009).
68. L. V. Zhigilei, B. J. Garrison, "Microscopic simulation of short pulse laser damage of melanin particles". *Laser-Tissue Interaction IX, Proceedings of SPIE*, 135–143 (1998).
69. D. D. Ho, R. London, G. B. Zimmerman, D. A. Young, Laser-tattoo removal–A study of the mechanism and the optimal treatment strategy via computer simulations. *Lasers Surg. Med.* **30**, 389–397 (2002).
70. J. Neumann, R. Brinkmann, Nucleation dynamics around single microabsorbers in water heated by nanosecond laser irradiation. *J. Appl. Phys.* **101**, 114701 (2007).
71. Chemical Rubber Company, *CRC Handbook of Chemistry and Physics*, (CRC Press, Taylor & Francis, Boca Raton, FL, 2020).
72. Q. Sun *et al*., *In vivo* imaging-guided microsurgery based on femtosecond laser produced new fluorescent compounds in biological tissues. *Biomed. Opt. Express* **9**, 581–590 (2018).
73. Z. Qin *et al*., New fluorescent compounds produced by femtosecond laser surgery in biological tissues: The mechanisms. *Biomed. Opt. Express* **9**, 3373–3390 (2018).
74. D. M. Simanovskii *et al*., Cellular tolerance to pulsed hyperthermia. *Phys. Rev. E Stat. Nonlin. Soft Matter Phys.* **74**, 011915 (2006).
75. A. Maeda, T. Maeda, M. Golczak, K. Palczewski, Retinopathy in mice induced by disrupted all-trans-retinal clearance. *J. Biol. Chem.* **283**, 26684–26693 (2008).
76. A. Maeda *et al*., Role of photoreceptor-specific retinol dehydrogenase in the retinoid cycle in vivo. *J. Biol. Chem.* **280**, 18822–18832 (2005).
77. L. A. J. Alvarez *et al*., SP8 FALCON: A novel concept in fluorescence lifetime imaging enabling video-rate confocal FLIM. *Nat. Methods* **16**, 1069–1071 (2019).
78. L. Malacrida *et al*., Spectral phasor analysis of LAURDAN fluorescence in live A549 lung cells to study the hydration and time evolution of intracellular lamellar body-like structures. *Biochim. Biophys. Acta* **1858**, 2625–2635 (2016).